Reaction mechanisms and multifragmentation processes in $^{64}Zn+^{58}Ni$ at $35A-79A$ MeV

R. Wada, K. Hagel, J. Cibor, M. Gonin,* Th. Keutgen, M. Murray, and J. B. Natowitz
Cyclotron Institute, Texas A&M University, College Station, Texas 77843

A. Ono
Department of Physics, Tohoku University, Sendai 980-8578, Japan

J. C. Steckmeyer,[1] A. Kerambrum,[1] J. C. Angélique,[1] A. Auger,[2] G. Bizard,[1] R. Brou,[1] C. Cabot,[2,†] E. Crema,[2,‡] D. Cussol,[1] D. Durand,[1] Y. El Masri,[3] P. Eudes,[4] Z. Y. He,[1,§] S. C. Jeong,[1,‖] C. Lebrun,[4] J. P. Patry,[1] A. Péghaire,[2] J. Peter,[1] R. Régimbart,[1] E. Rosato,[5] F. Saint-Laurent,[2] B. Tamain,[1] and E. Vient[1]

(The GANIL E-160 Collaboration)
[1]*LPC, IN2P3-CNRS, ISMRA et Université, F-14050 Caen Cedex, France*
[2]*GANIL, DSM-CEA, IN2P3-CNRS, BP 5027, F-14076 Caen Cedex 05, France*
[3]*IPN, FNRS, Université Catholique de Louvain, B-1348 Louvain-Neuve, Belgium*
[4]*SUBATECH, Université de Nantes, IN2P3-CNRS, F-44070 Nantes Cedex 03, France*
[5]*Dipartimonto di Scienze Fisiche, Universita di Napoli, I-80126 Napoli, Italy*
(Received 4 February 2000; published 26 July 2000)

Reaction mechanisms and multifragmentation processes have been studied for $^{64}Zn+^{58}Ni$ collisions at intermediate energies with the help of antisymmetrized molecular dynamics (AMD-V) model calculations. Experimental energy spectra, angular distributions, charge distributions, and isotope distributions, classified by their associated charged particle multiplicities, are compared with the results of the AMD-V calculations. In general the experimental results are reasonably well reproduced by the calculations. The multifragmentation observed experimentally at all incident energies is also reproduced by the AMD-V calculations. A detailed study of AMD-V events reveals that, in nucleon transport, the reaction shows some transparency, whereas in energy transport the reaction is much less transparent at all incident energies studied here. The transparency in the nucleon transport indicates that, even for central collisions, about 75% of the projectile nucleons appear in the forward direction. In energy transport about 80% of the initial kinetic energy of the projectile in the center-of-mass frame is dissipated. The detailed study of AMD-V events also elucidates the dynamics of the multifragmentation process. The study suggests that, at $35A$ MeV, the semitransparency and thermal expansion are the dominant mechanisms for the multifragmentation process, whereas at $49A$ MeV and higher incident energies a nuclear compression occurs at an early stage of the reaction and plays an important role in the multifragmentation process in addition to that of the thermal expansion and the semitransparency.

PACS number(s): 25.70.Pq, 02.70.Ns, 24.10.Lx

I. INTRODUCTION

Heavy ion reactions in the intermediate energy domain of 10 MeV/nucleon to a few GeV/nucleon have been used to explore the nature of nuclei at the limits of their stability in temperature and excitation energy [1–7]. In these studies characterization of the initial hot composite system is very crucial. Significant experimental efforts have been devoted to evaluating the characteristic properties of the initial hot composite system, such as the charge, excitation energy, and temperature, by reconstruction from the experimental observables, but large ambiguities remain in the extracted values [7–10]. The interpretation of the derived parameters is also very difficult without an understanding of the reaction dynamics involved. The multifragmentation process has been often studied using models, such as the statistical multifragmentation model (SMM) [11–13], or the expanding emitting source (EES) model [14]. In these simulations only the later stage of the multifragmentation process is treated. Without a treatment of the dynamics of the entrance channel, a large uncertainty can remain in the final results.

In order to establish the reaction dynamics, intensive theoretical efforts have been made in developing microscopic models [15]. The Boltzmann-Uehling-Uhlenbeck (BUU), the Vlasov-Uehling-Uhlenbeck (VUU) models [2,16,17], the quantum molecular dynamics (QMD) model [4,18–20], and the antisymmetrized or fermionic molecular dynamics models (AMD or FMD) [21–23] have been developed and compared with experimental results. For central collisions some of these models predict the formation of a hot composite system at the early stage of the reaction. Experimentally,

*Permanent address: LPHNE-X, Ecole Polytechnique, 91128 Palaiseau Cedex, France.
†Permanent address: Institut de Physique Nucléaire, IN2P3-CNRS, 91406 Orsay Cedex, France.
‡Permanent address: Instituto de Fisica, Universidade de São Paulo, CP 20516, 01498 São Paulo, Brazil.
§Permanent address: IMP, Chinese Academy of Sciences, Lanzhou 730000, People's Republic of China.
‖Present address: Institute of Nuclear Studies, University of Tokyo, Tokyo, Japan.

some evidence has been reported for the formation of such a single hot source for central collisions [7–9]. On the other hand, a dominant binary nature has also been reported for symmetric light and medium mass systems [24]. Recently semitransparency has been suggested in the QMD calculations even for the central collisions in the Xe+Sn reaction at 50*A* MeV by Nebauer and Aichelin [20] and in the AMD calculations on ^{40}Ca+^{40}Ca at 35*A* MeV by Wada *et al.* [22]. Good agreement between the results of the latter experiment and the calculations strongly supports the existence of some transparency in that system.

In this paper we investigate the reaction mechanism and multifragmentation process of the ^{64}Zn+^{58}Ni reaction at 35*A*–79*A* MeV by comparing the experimental results to the calculated results obtained with the AMD model. In Sec. II the experiment is described. In Sec. III a brief description of the AMD approach is presented. Section IV is devoted to presenting the experimental and calculated results. In Sec. V the reaction mechanism and the multifragmentation process are discussed and the AMD events are investigated in detail. In Sec. VI a summary is given.

II. EXPERIMENT

The experiment was performed at the GANIL (Grand Accélérateur National d'Ions Lourds) facility in France, using a 4π detector array. ^{64}Zn projectiles were incident on a ^{58}Ni target with an areal density of 340 μg/cm^2 at energies of 35*A*, 49*A*, 57*A*, 69*A*, and 79*A* MeV. Charged particles with $Z\leqslant 8$ were detected by a 4π detector, consisting of two plastic multidetector arrays, MUR and TONNEAU [25,26]. The arrays cover a total solid angle of 84% of 4π. MUR consists of 96 pads of plastic scintillator (NE102A), 2 mm thick, and was located at a distance of 210 cm from the target in seven concentric rings, covering an angular range between 3° and 30°. TONNEAU consists of two parts, forward (30°–90°) and backward (90°–150°). Each part consists of 36 plastic scintillator rods (2 mm thick) at a distance of 83 cm from the target and signals at both ends are read in each rod for the determination of the polar emission angle. Identification of $Z=1$ and 2 particles was made possible by the ΔE (or E) versus the time-of-flight (TOF) method for particles with energy above 2.5*A* MeV. Identification of fragments ($3\leqslant Z\leqslant 8$) was only possible for energies above 15*A*–20*A* MeV in these detector arrays. The velocities of the identified particles were determined from the TOF and the flight distances.

In addition to the intermediate mass fragments (IMFs) detected in the plastic multidetector arrays, fragments with $Z\geqslant 4$ were measured by seven Si telescopes set in front of MUR, five at polar angles of $\theta=4.3°$, 7.3°, 10.9°, 16.0°, 22.0°, and two at $\theta=28.5°$. The telescopes shadowed MUR in the azimuthal angle range of $\Delta\phi=22.5°$ (6.3% of the MUR coverage). The telescopes consisted of ΔE (300 or 500 μm) and E (6.0 or 3.5 mm) Si detectors. The charges of all detected fragments in the telescopes were clearly identified above an energy threshold of 15*A*–20*A* MeV and isotopes for $4\leqslant Z\leqslant 7$ were also identified at $\theta\geqslant 16°$. Absolute energy calibration of the silicon detectors was performed by measuring directly the particles produced in the ^{16}O+^{12}C reaction at 95*A* MeV. Particles with a projectilelike velocity of a fixed ratio of P/Q (P is momentum and Q is charge state) were delivered directly to the telescopes using a bending magnet. All isotopes from $Z=3$ to $Z=8$ were clearly observed and the absolute energy of each isotope was determined from the field strength of the magnet. The ΔE and E detectors of each telescope were calibrated using all measured isotopes with a given energy and range-energy tables [27].

III. MODEL SIMULATIONS

A. AMD model

Experimental results have been compared with antisymmetrized molecular dynamics model calculations [21,28,29]. In AMD a reaction system with N nucleons is described by a wave function which is a single Slater determinant of N Gaussian wave packets,

$$\Phi(Z)=\det\left[\exp\left\{-\nu\left(\mathbf{r}_j-\frac{\mathbf{Z}_i}{\sqrt{\nu}}\right)^2+\frac{1}{2}\mathbf{Z}_i^2\right\}\chi_{\alpha_i}(j)\right], \quad (1)$$

where the complex variables $Z\equiv\{\mathbf{Z}_i;i=1,\ldots,N\}=\{Z_{i\sigma};\ i=1,\ldots,N,\ \sigma=x,y,z\}$ represent the centroids of the wave packets. The width parameter ν is taken as $\nu=0.16$ fm^{-2} and χ_{α_i} represents the spin and isospin states of $p\uparrow$, $p\downarrow$, $n\uparrow$, or $n\downarrow$. The time evolution of Z is determined by the time-dependent variational principle and the two-nucleon collision process. The equation of motion for Z derived from the time-dependent variational principle is

$$i\hbar\sum_{j\tau} C_{i\sigma,j\tau}\frac{dZ_{j\tau}}{dt}=\frac{\partial\mathcal{H}}{\partial Z_{i\sigma}^*}. \quad (2)$$

$C_{i\sigma,j\tau}$ is a Hermitian matrix defined by

$$C_{i\sigma,j\tau}=\frac{\partial^2}{\partial Z_{i\sigma}^*\partial Z_{j\tau}}\ln\langle\Phi(Z)|\Phi(Z)\rangle, \quad (3)$$

and $\mathcal{H}$ is the expectation value of the Hamiltonian after the subtraction of the spurious kinetic energy of the zero-point oscillation of the center of masses of fragments [28]. Two nucleon collisions are introduced by the use of the physical coordinates $\mathrm{W}\equiv\{W_i\}$ which are defined as

$$\mathbf{W}_i=\sum_{j=1}^{A}(\sqrt{Q})_{ij}\mathbf{Z}_i, \quad (4)$$

and Q_{ij} is defined as

$$Q_{ij}=\frac{\partial}{\partial(\mathbf{Z}_i^*\cdot\mathbf{Z}_j)}\ln\langle\Phi(Z)|\Phi(Z)\rangle. \quad (5)$$

In molecular dynamics models with Gaussian wave packets, the ith nucleon at time $t=t_0$ is represented in phase space by

$$f_i(\mathbf{r},\mathbf{p},t_0)=8\exp\left\{-2\nu(\mathbf{r}-\mathbf{R}_i(t_0))^2-\frac{(\mathbf{p}-\mathbf{P}_i(t_0))^2}{2\hbar^2\nu}\right\}, \tag{6}$$

with the centroid $\mathbf{R}_i$ and $\mathbf{P}_i$. The total one-body distribution function is the sum of f_i. In the AMD model, this representation of a nucleon as a simple Gaussian wave packet is valid only approximately when the physical coordinate

$$\mathbf{W}_i=\sqrt{\nu}\mathbf{R}_i+\frac{i}{2\hbar\sqrt{\nu}}\mathbf{P}_i \tag{7}$$

is used for the centroids [28].

In order to treat properly the reactions with many branching channels such as multifragmentation processes discussed in this paper, the AMD model has been extended by introducing the wave packet diffusion effect as a quantum branching process. This extended AMD model is called the AMD-V model, since the wave packet diffusion effect is calculated with the Vlasov equation [21]. The AMD-V model has been successfully applied to the multifragment events in the ^{40}Ca+^{40}Ca reaction at 35*A* MeV [21,22]. The AMD-V code has been further improved in order to save CPU time in the numerical calculations and to be applicable to heavier reaction systems [29]. In the newly developed code, used for all calculations in this paper, the wave packet diffusion effect calculation has been reformulated and a triple-loop approximation, discussed in Ref. [29], has been incorporated.

For the ^{64}Zn+^{58}Ni reaction, about 3000 events were generated at each energy in an impact parameter range of 0–12 fm. The calculations were performed in the VPP700E supercomputer facility in Riken, Japan. The Gogny force [30], which gave the best fit in the previous analysis of ^{40}Ca +^{40}Ca at 35*A* MeV [21,22], was used as an effective interaction in these calculations. The Gogny force gives an incompressibility of 228 MeV for infinite nuclear matter and a momentum-dependent mean field. The calculations started at a distance of 15 fm between two centers of the projectile and target in the beam direction. Each event was calculated up to $t=300$ fm/c in most cases and up to 500 fm/c for a few cases. At 300 fm/c the excitation energies and momenta of fragments are evaluated. Fragments are identified using a coalescence technique with a coalescence radius of 5 fm, but the size of the fragments at $t=300$ fm/c depends only slightly on the coalescence radius for these incident energies, because the system already breaks into small pieces at this time for all the cases.

B. Afterburner and switching time

The generated fragments in the AMD-V model are generally in an excited state at a time of 300 fm/c and a very long CPU time is needed for the fragments to cool down to the ground state. Instead of continuing the AMD-V calculation, the calculation was stopped at $t=300$ fm/c (which corresponds to a realistic CPU time to get a few thousand events in the VPP700E) and the fragments were cooled, using a statistical decay code as an afterburner. A modified version of GEMINI [32] was used as the afterburner. In this modified version, discrete levels of the excited states of light fragments with $Z\leqslant 14$ are taken into account and the Hauser-Feshbach formalism is extended to the particle decay from a parent nucleus with $Z\leqslant 20$ when the excitation energy of the parent nucleus is below 50 MeV. One AMD-V event is used 100 times in the afterburner in order to sample all possible decay paths of the excited fragments, which also gives enough statistics for detailed comparisons to the experimental results. All calculated AMD-V results have been filtered through the experimental conditions, such as the detector coverage and energy thresholds, unless otherwise specified.

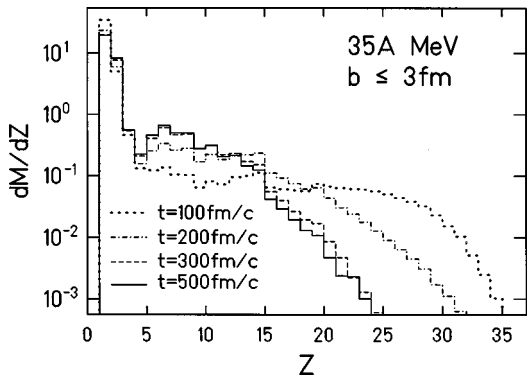

FIG. 1. Final calculated charge distributions at 35*A* MeV are compared for the different choices of the switching time to the afterburner. Represented by different line types, the results are shown as histograms as indicated in the figure. The results are not filtered by the experimental conditions.

The switching time of $t=300$ fm/c is chosen only for the technical reason of the computation time in the VPP700E. In the AMD-V simulations, the later the switching time is, the more preferable, because the particle evaporation occurs in the quantum statistical manner [31]. For the reactions studied here, the switching time of $t=300$ fm/c is late enough so that the final results do not depend significantly on the choices of the switching time after this time. In Fig. 1 the final charge distributions calculated for the different switching times are shown at 35*A* MeV. In this plot the central events with the impact parameter $b\leqslant 3$ fm are used and no experimental filter is applied. Significant differences are observed between the switching times of $t=100$ fm/c and $t=300$ fm/c, whereas no significant differences are observed after $t=300$ fm/c. At higher incident energies, the final results become independent after $t\sim 200$ fm/c, because the reaction process becomes faster at the higher incident energies. The large difference in the final charge distributions indicates, as discussed in later sections, that the fragmentation process in the early stages is significantly affected by the dynamical reaction process.

IV. RESULTS

A. Reaction cross sections and multiplicity distributions

In Fig. 2 charged particle multiplicities detected in the plastic arrays are shown at three different incident energies. In the experimental results, most events with multiplicity

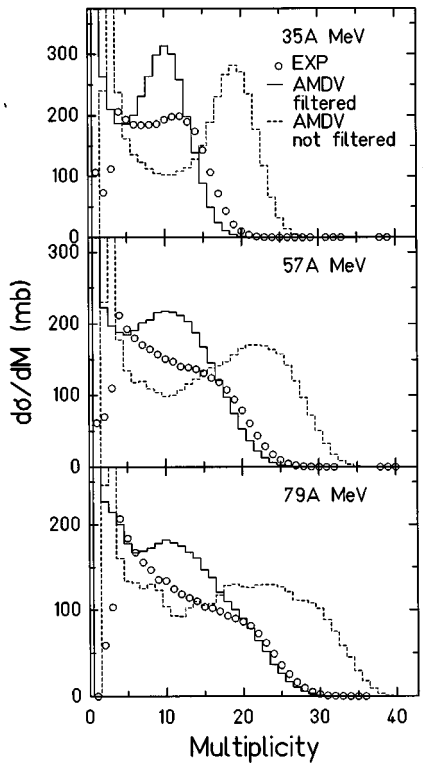

FIG. 2. Multiplicity distributions of the charged particles in the plastic arrays at 35*A* MeV (top), 57*A* MeV (middle), and 79*A* MeV (bottom) are compared for the experimental results (circles) and the AMD-V calculations (histograms) on an absolute scale. For the calculated distributions, both filtered and nonfiltered distributions are shown. The filtered distributions are obtained by filtering the events through the experimental conditions and plotted by solid line histograms. The nonfiltered distributions are shown by the dashed line histograms.

$M \leqslant 3$ were rejected by the hardware trigger during the experiment. The experimental absolute cross sections are calculated from the integrated beam current in the Faraday cup, assuming that the projectiles are fully stripped in the target and no electrons go into the Faraday cup. The accuracy of this method should be better than 10% [33]. The cross sections in the AMD-V calculations are determined by the impact parameter range used. For the calculated results the filtered and nonfiltered distributions are shown by solid and dashed line histograms, respectively. The overall detection efficiency of the charged particles in the experiment is about 60%. For charged particle multiplicities around $M \sim 10$, the calculated AMD-V results overestimate the cross section for all incident energies, as seen by comparing the experimental results and the calculated filtered distributions (solid line histograms). As seen later, this excess yield originates from the collisions with the impact parameter $b \sim 7-8$ fm, which corresponds to about twice of the mean square radius of the initial nuclei. This suggests that the excess yield relates closely to the nuclear surface properties during the collisions. For the initial nuclei, however, the mean square radii are $R_{rms} = 3.83$ and 3.76 for ^{64}Zn and ^{58}Ni, respectively, and are comparable to the experimental values (3.95 and 3.77, respectively) determined by electron elastic scattering [34].

TABLE I. Reaction cross section.

E_{inc} (*A* MeV)	Expt. ($M \geqslant 4$) (mb)	AMD-V ($M \geqslant 4$) (mb)
35	2496	2756
49	2517	2922
57	2615	2959
69	2737	2998
79	2534	2852

This excess yield turns out to be caused by the approximation used to calculate the physical coordinate when two-nucleon collisions are examined. The two-nucleon collisions are evaluated in the physical coordinate space, using the approximated physical coordinate $\{W_i\}$ in Eq. (4). The density calculated in the physical coordinate space, however, shows a slightly larger radius than that of the exact calculation. Since the peripheral collisions are significantly affected by the two-nucleon collisions at the nuclear surface, this approximation results in a significant effect on the collisions with the impact parameter corresponding to the sum of the nuclear radius of the projectile and the target. A more detailed discussion of problems in the calculation will be given in Sec. V. In Table I, a summary of the measured reaction cross sections for $M \geqslant 4$ is given for the experiment and the calculations. The calculated cross sections are about 10–15 % larger than those of the experiment for all incident energies.

B. Event classification for centrality

In Fig. 3 the parallel velocity distributions of $Z=1$ and $Z=2$ particles, detected in the plastic arrays, are shown for different charged particle multiplicity windows. For the lowest multiplicity window (top row), a two-peak structure is clearly observed at 57*A* and 79*A* MeV for both $Z=1$ and $Z=2$ particles. The peak velocity corresponding to the higher peak is about 90–95 % of the beam velocity and the lower one is near 2 cm/ns. This indicates that the higher component originates from a projectilelike source and the lower component originates from a targetlike source in binary-type collisions. The velocity distribution near the slower peak is distorted by the experimental conditions. The shoulder at $V_{\|} \sim 0$ cm/ns for $Z=1$ is caused by the shadow of the target frame, and the asymmetry of the two peaks for $Z=2$ is caused by the detector energy thresholds of the plastic arrays as well as the shadowing by the target frame. The two-peak structure for both particles gradually merges into a broad single bump when the multiplicity increases, suggesting that the reaction becomes more violent and the contribution from an intermediate velocity source becomes important as the multiplicity increases. This characteristic feature is less prominent at 35*A* MeV, but one can still see the evolution in the width of the velocity distribution. The width becomes narrower as the multiplicity increases. The evolution of the parallel velocity distribution with multiplicity indicates that the charged particle multiplicity can be used as a reasonable probe for the impact parameter. Calculated results from the AMD-V model are also shown by histograms in the

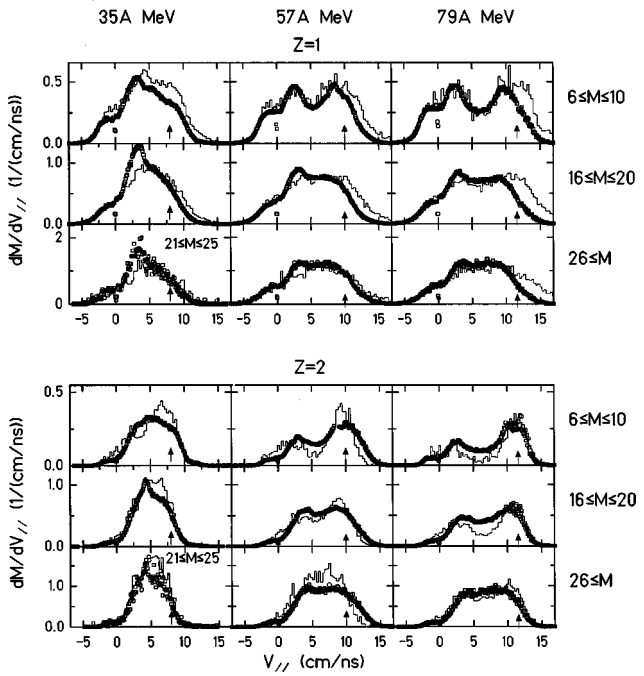

FIG. 3. Parallel velocity distributions of $Z=1$ (upper) and $Z=2$ (lower) particles in the plastic arrays are plotted for different charged particle multiplicity windows at 35*A* MeV (left), 57*A* MeV (middle), and 79*A* MeV (right). The experimental results are shown by squares and those from the AMD-V calculations are shown by histograms. The range of the charged particle multiplicity window used is indicated on the right, except for the highest multiplicity window at 35*A* MeV. The arrow on the x axis in each figure indicates the velocity of the projectile. The vertical scale is the absolute multiplicity per unit parallel velocity both in the experimental and calculated results.

figure. The evolution of the shape of the distribution in the different multiplicity windows is very well reproduced, including the distortions by the experimental conditions. The calculated velocity distributions, however, show a slightly higher velocity component for $Z=1$, which is not seen in the experimental distributions. The relative yields of protons and alpha particles are also reasonably reproduced, although the sum of the proton number and the α particle number is restricted by the given multiplicity range.

In Fig. 4 summed transverse momenta of the charged particles detected in the plastic arrays are shown for the different multiplicity windows. The transverse momentum is calculated by assuming mass $A=1$ for $Z=1$, $A=2Z$ for $Z \geqslant 2$ both in the experimental and calculated results. The summed momentum is scaled by the beam momentum. The evolution of the peak momentum and the width of the distributions becomes very similar between different incident energies. The peak positions and widths of the distributions increase systematically as the multiplicity increases. The experimental peak positions and shapes in the different multiplicity windows are well reproduced by the calculations (solid line histograms). In each figure the calculated results without filtering are also shown by dashed line histograms. In general the peak position and width of the distributions in the nonfiltered distributions evolve similarly to the filtered

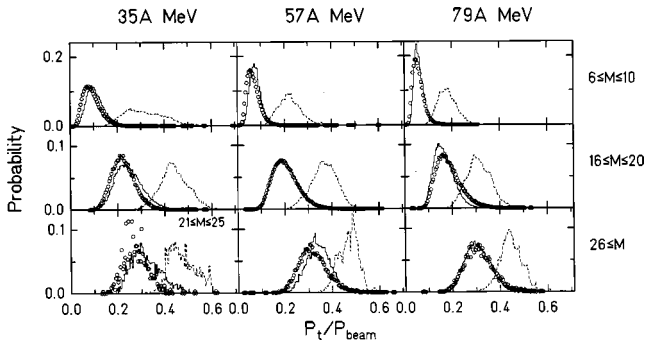

FIG. 4. Summed transverse momentum distributions of the charged particles detected in the plastic arrays are plotted for different charged particle multiplicity windows at three different incident energies. The incident energy is indicated at the top of each column. The range used for the multiplicity window is given on the left, except for the highest multiplicity window at 35*A* MeV. The experimental results are shown by circles. The calculated results are shown both for the filtered distribution (solid line histograms) and for nonfiltered distributions (dashed line histograms).

distributions. The average values of the summed transverse momenta for the different multiplicity windows are summarized in Table II both for the experiment and for the calculations at all incident energies. In the calculated results, transverse momenta from the filtered and nonfiltered events are given. One can clearly see good agreement between the experimental values and the calculated filtered values for the different particle multiplicity windows at all incident energies. For the highest multiplicity window about 70% of the transverse momentum, remains in the filtered events, whereas for the lowest multiplicity window only 20% of the transverse momentum remains after filtering the events.

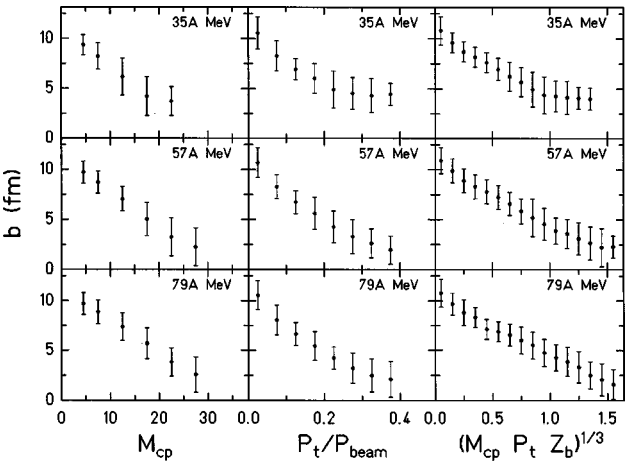

FIG. 5. Correlations between the impact parameter and the charged particle multiplicity (left), the summed transverse momentum (middle), and a combined parameter (right) in the calculations for different incident energies. The incident energy is indicated in each figure. Dots indicate the centroid of the distribution and bars indicate the FWHM of the distribution. For the combined parameter, the charged particle multiplicity, the summed momentum, and the Z bound are scaled by $M=30$, P_{beam}, and $Z_{tot}=58$, respectively.

TABLE II. Average summed transverse momentum. The values are scaled by the incident beam momentum at each energy.

	Multiplicity range					
	4–5	6–10	11–15	16–20	20–25	26⩽
35*A* MeV						
Expt.	0.039	0.092	0.163	0.220	0.268	
AMD-V (filtered)	0.040	0.103	0.168	0.241	0.310	
AMD-V (not filtered)	0.224	0.309	0.379	0.433	0.465	
49*A* MeV						
Expt.	0.034	0.079	0.145	0.215	0.268	0.308
AMD-V (filtered)	0.027	0.070	0.145	0.220	0.288	0.361
AMD-V (not filtered)	0.148	0.236	0.347	0.414	0.456	0.498
59*A* MeV						
Expt.	0.031	0.063	0.125	0.199	0.263	0.313
AMD-V (filtered)	0.031	0.071	0.122	0.195	0.268	0.330
AMD-V (not filtered)	0.168	0.217	0.282	0.359	0.417	0.460
69*A* MeV						
Expt.	0.030	0.060	0.124	0.195	0.263	0.317
AMD-V (filtered)	0.022	0.055	0.116	0.191	0.251	0.300
AMD-V (not filtered)	0.122	0.188	0.287	0.374	0.424	0.457
79*A* MeV						
Expt.	0.027	0.054	0.108	0.180	0.253	0.304
AMD-V (filtered)	0.020	0.054	0.098	0.152	0.232	0.299
AMD-V (not filtered)	0.123	0.174	0.233	0.304	0.379	0.437

These observations suggest that the summed transverse momentum, as well as the charged particle multiplicity, may be used as a probe for the centrality of collisions. Since the AMD-V results are in good agreement with the experimental parallel velocity and summed transverse momentum distributions, the correlations between these observables and the impact parameter can reasonably be studied in the calculations. In Fig. 5 the calculated average impact parameter is plotted as a function of the filtered charged particle multiplicity on the left column and as a function of the transverse momentum in the middle. On the right a combined parameter is used [35], which consists of the charged particle multiplicity, transverse momentum, and the summed charge of the fragments with $Z \geqslant 2$ (Z bound). Impact parameter distributions in a given parameter range show a broad distribution of full width at half maximum (FWHM) $\sim 3-4$ fm for the most central events in all cases. At 35*A* MeV the impact parameter decreases to 4 fm as the charged particle multiplicity increases up to 17.5 and becomes more or less constant after that. This situation is similar for the other two observables. The impact parameter range for the most central collisions, which one can probe using these parameters, is around 0–5 fm. One can select a slightly narrower impact parameter range at higher incident energies. No significant difference in probing the impact parameter is observed for the three different parameters studied here. In the following sections, therefore, the charged particle multiplicity is used to classify events according to centralities for simplicity.

C. IMF energy spectra

Typical IMF energy spectra measured by the telescopes are shown in Fig. 6 for $Z=6$ at 35*A* MeV and $Z=8$ at 57*A* MeV. Energy spectra at different laboratory angles are plotted for different associated charged particle multiplicity windows. An interesting observation for the energy spectra is that only small differences are observed in the shapes and angular dependences of the energy spectra in the different multiplicity windows. At 35*A* MeV, the energy spectra at the lowest multiplicity window (circles) show a slight enhancement at two forward angles at $E_{lab} \sim 400$ MeV, which is near the projectile velocity, but at $\theta \geqslant 10.9°$ the spectra become very similar to those in the other two multiplicity windows. At 57*A* MeV the shapes and angular dependences of the spectra are very similar to each other for all of the multiplicity windows. Since the energy spectra are rather independent of the impact parameter and the statistics in the calculations are not so high, energy spectra are compared to the calculated results without classification by the associated charged particle multiplicity.

Typical inclusive energy spectra of IMFs are plotted for 35*A*, 49*A*, and 57*A* MeV in Figs. 7–9. The calculated spectra are not filtered for the energy thresholds in order to see the entire calculated energy spectrum at a given angle. Fine structures in the calculated results are statistical fluctuations. Experimental energy spectra have rather high thresholds ($\sim 15-20\,A$ MeV) and a significant part of the low en-

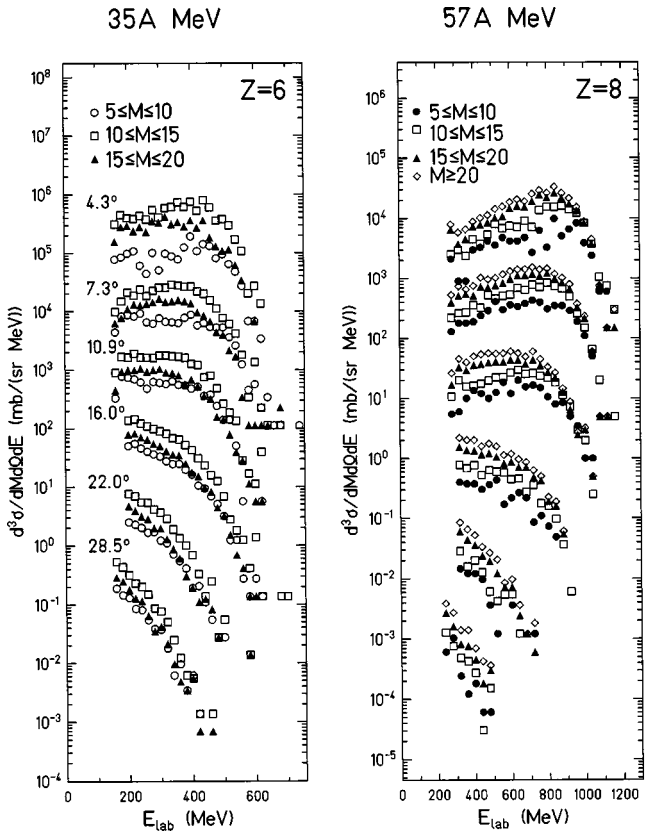

FIG. 6. Experimental energy spectra of $Z=6$ at 35A MeV (left) and $Z=8$ at 57A MeV (right) at different angles, measured by the telescopes, are shown for different charged particle multiplicity windows. Spectra for different multiplicity windows are shown by different symbols indicated in each figure. Angles are also indicated in the left figure. Each spectrum is plotted in an absolute differential cross section. The spectra are multiplied by factor of 10^n ($n=0,1,2,3,4,5$) from the bottom to the top.

zergy side of the spectrum is cut off for $Z \geqslant 8$ at the larger angles. At the incident energies above 49A MeV, some light IMFs start to punch through the E detector of the telescopes at forward angles and no identification is made above that energy. In general the energy spectra are reproduced reasonably well in shape and amplitude at all incident energies. There are, however, a few disagreements. At 35A MeV the cross section of $Z=4$ is significantly underestimated, especially at the low energy side, at all angles. This trend is also observed less prominantly in the spectra for $Z=5$. For heavier fragments the experimental spectra are well reproduced except at $\theta=4.3°$, in which the peak energy in the calculated spectra is about 20–30 % lower than that in the experimental results. At higher incident energies, the calculated cross section for $Z=5$ shows a similar trend to that at 35A MeV. For the heavier fragments, the spectra at forward angles are well reproduced, whereas the calculated cross sections at $\theta=10.9°$ and $\theta=16.0°$, especially at 49A MeV, show a systematic shift toward the higher energy side.

D. IMF angular distribution

Energy-integrated angular distributions of IMFs are studied in different charged particle multiplicity windows. Energy spectra are integrated above the thresholds at each angle. For some of the light IMFs the energy integration has an upper limit because of the punch through in the E detector at forward angles. The same energy integration limits are used for integrating the calculated energy spectra. The experimental and calculated angular distributions for some of IMFs are shown in Fig. 10 for 35A MeV and Fig. 11 for

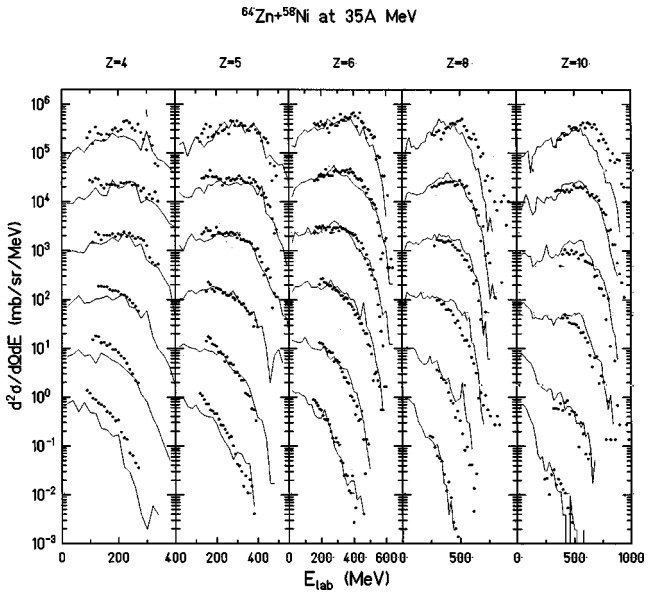

FIG. 7. Typical IMF energy spectra measured by the telescopes at 35A MeV are shown for different IMFs. The charge of the IMF is given at the top of the figure. Spectra from the top to the bottom correspond to those at $\theta=4.3°$, 7.3°, 10.9°, 16.0°, 22.0°, and 28.5°. The experimental results (dots) and calculated results (histograms) are plotted as absolute differential cross sections. The spectra are multiplied by a factor of 10^n ($n=0,1,2,3,4,5$) from the bottom to the top.

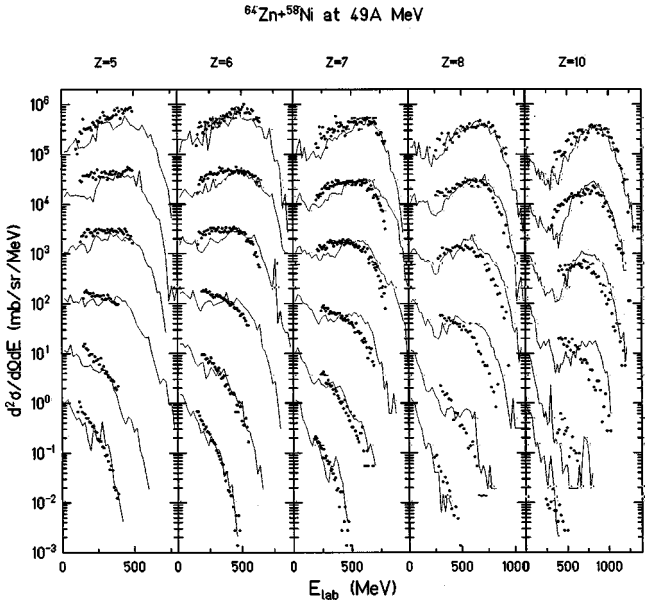

FIG. 8. Similar plots to those in Fig. 7, but at 49A MeV. See also the caption in Fig. 7.

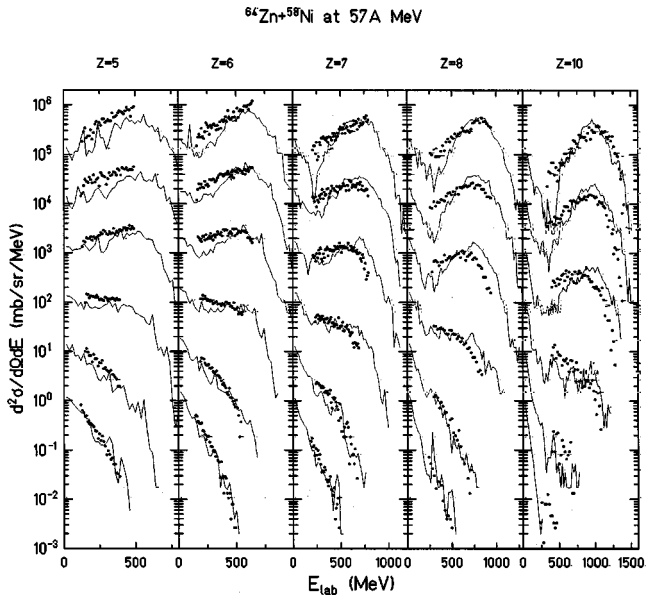

FIG. 9. Similar plots to those in Fig. 7, but at 57*A* MeV. See also the caption in Fig. 7.

49*A* MeV and 57*A* MeV. The experimental angular distributions show a peak around 7°–10°. The magnitude of the distribution increases generally with increasing multiplicity except for those in the higher multiplicity windows. The decrease of the magnitude, especially for the heavier IMFs, in

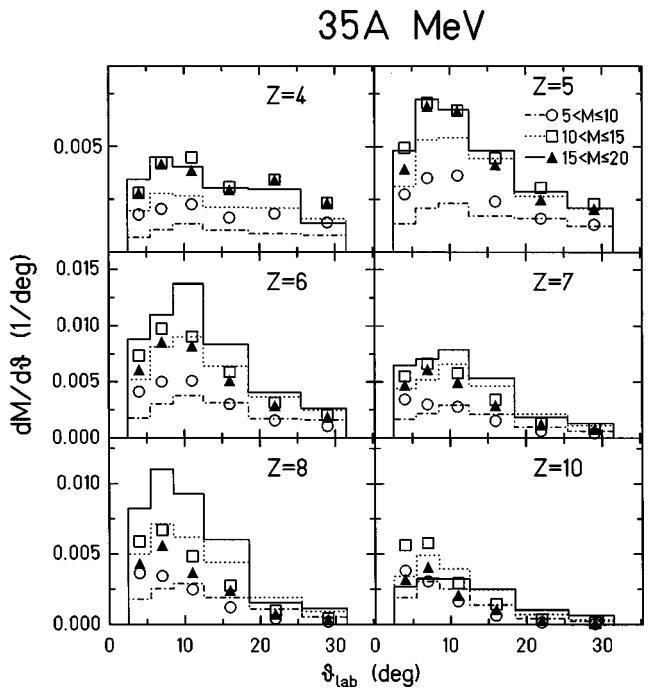

FIG. 10. Energy-integrated angular distributions for some IMFs at 35*A* MeV are plotted for different charged particle multiplicity windows. The experimental results are shown by symbols and the calculated distributions are shown by histograms. Results for the different multiplicity windows are shown by different symbols and lines, indicated in the top right figure. The vertical scale is the absolute differential multiplicity in both cases.

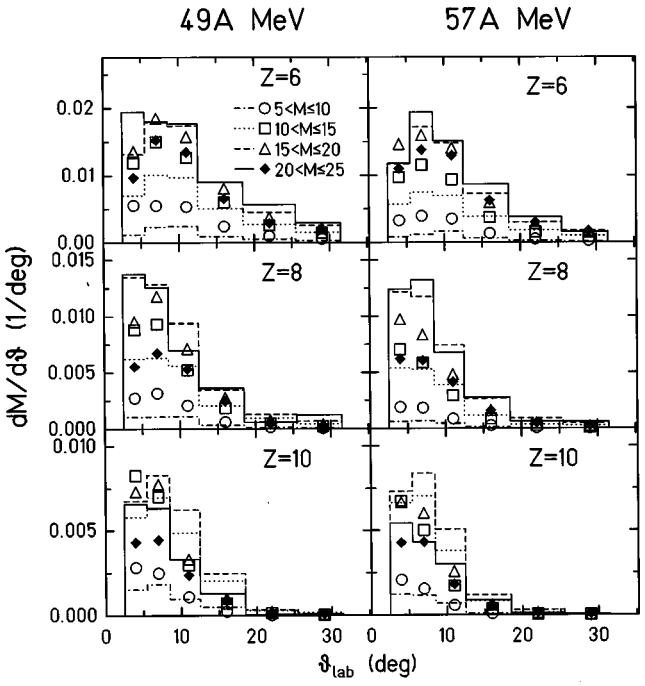

FIG. 11. Similar plots to those in Fig. 10, but at 49*A* MeV on the left and 57*A* MeV on the right. The same multiplicity windows are applied at both energies. See also the caption in Fig. 10.

the higher multiplicity windows is simply caused by charge conservation in each event. For the high multiplicity events, the whole system is fragmented into small pieces and the large fragments are less abundant. The calculated angular distributions show a similar trend in the evolution of the magnitude of the distribution for the different multiplicity windows.

One should note that the shapes of the angular distributions plotted in Figs. 10 and 11 are distorted significantly by the experimental conditions. Most of the fragments emitted at larger angles are not detected in the experiment and filtered out in the calculations because of the energy threshold of the telescopes. In order to see the angular distribution of IMFs without the experimental conditions, the calculated momentum distributions of IMFs with $3 \leqslant Z \leqslant 10$ in the center-of-mass system are plotted in Fig. 12 for different impact parameter ranges at 57*A* MeV, without filtering the events. A two-peak structure is observed even for the very central collisions. This two-peak structure develops further when the impact parameter increases. Very similar features are observed at 35*A* MeV with a slightly less stretched distribution and at 79*A* MeV with a slightly more stretched distribution. This observation is also consistent to the results of ^{40}Ca+^{40}Ca at 35*A* MeV, where the angular distributions of IMFs in the center-of-mass system are directly compared with those of the calculation [22].

E. *Z* distribution

A total charge distribution of fragments has been obtained by integrating the spectra over energy and angle. The same experimental energy and angular ranges in the integration were used for the calculated spectra. The results are shown in

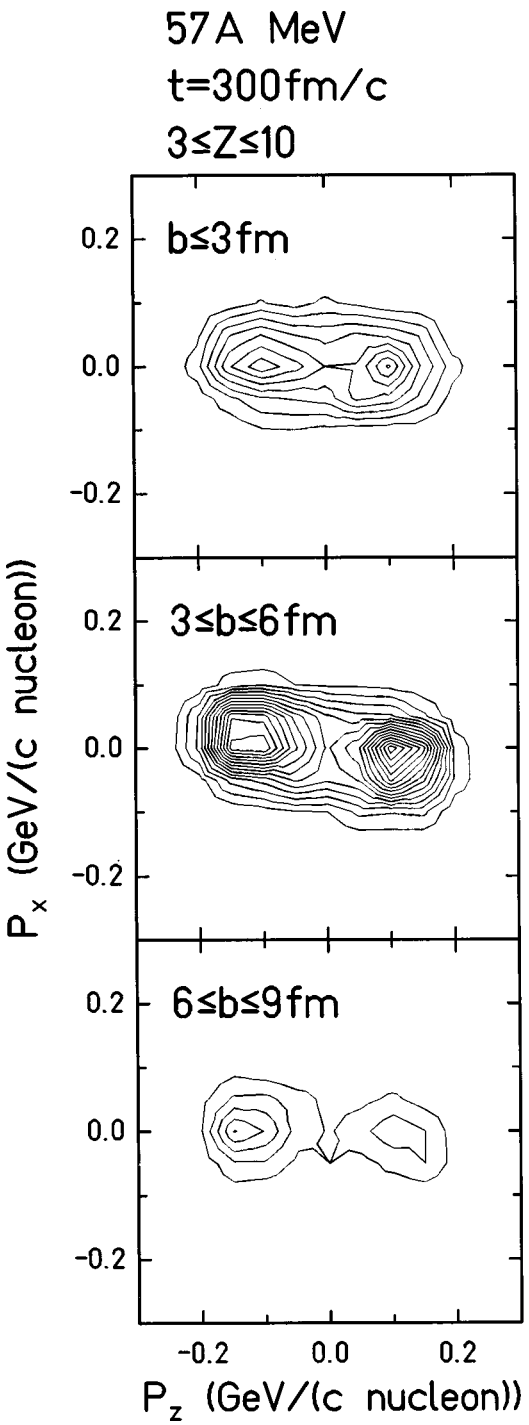

FIG. 12. Calculated average momentum distributions of IMFs with $Z=3-10$ at 57A MeV, projected on the reaction plane (X-Z plane) in the center-of-mass system, are plotted at $t=300$ fm/c for different impact parameter windows, indicated in each figure. The average momentum is given in GeV/(c nucleon).

Fig. 13 for different multiplicity windows at different incident energies. The evolution of the experimental charge distributions for different multiplicity windows is very well reproduced by the calculations at all incident energies, although the charge distributions for the lowest multiplicity window are rather poorly reproduced. The discrepancy in the lowest multiplicity window, seen in the plotted figures, is

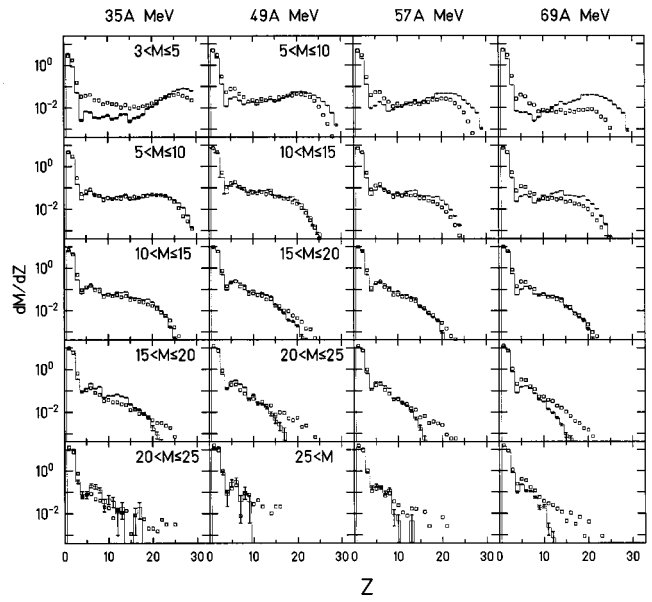

FIG. 13. Energy- and angle-integrated charge distributions for different charged particle multiplicity windows at different incident energies. The incident energy is indicated at the top of each column. The range of the multiplicity window applied is given in the figures for 35A MeV and 49A MeV. Those for the higher incident energies are the same as those for 49A MeV. Experimental results are shown by squares and the calculated results are shown by histograms. Both results are plotted as absolute multiplicity per unit charge. Errors indicate the statistical errors only for the calculated results. Experimental errors are smaller by a factor of 2–3 than those of the calculations at the same multiplicity.

similarly observed for those of the lowest multiplicity window at 49A and 57A MeV (not shown). The cause of this discrepancy will be discussed in the next section. For the higher multiplicity windows an excess of multiplicity is also generally observed near the largest IMF. This excess appears to be caused by accidental events, where two reactions occur in one beam burst. In such events one of the reactions has to be a violent collision to produce enough associated charged particles and the other is more likely to be a peripheral collision, which has a large cross section and likely has a large fragment. Such events have been largely eliminated by requiring momentum conservation, in which the sum of the parallel momenta of the observed charged particles is required to be less than the beam momentum. This procedure eliminates most of such events in the lower multiplicity windows, but not completely in the higher multiplicity windows.

F. Transverse energy spectra

In Fig. 14 typical inclusive transverse energy spectra of $Z=7$ and $Z=8$ at different incident energies are plotted for the experiment and the calculations. The transverse energy spectra are integrated over the detector angles. The experimental spectra show similar slopes at all incident energies, except in the higher energy side of $Z=7$ for the reaction at 35A MeV. The observed apparent slopes are around $T=20$ MeV. The general trend of the experimental spectra is well reproduced by the calculations. The AMD-V calcula-

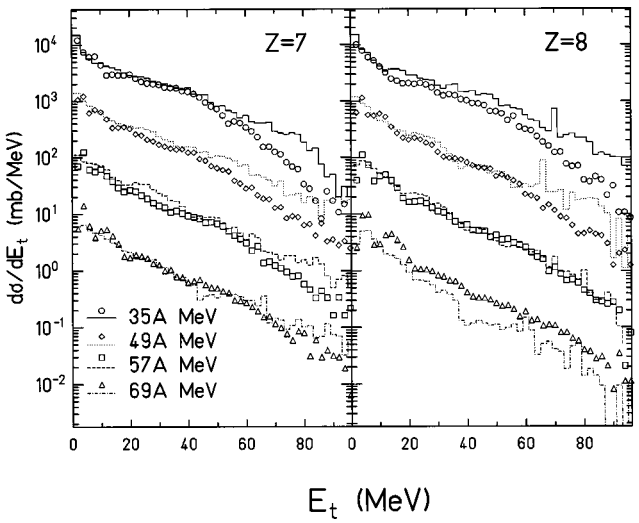

FIG. 14. Experimental and calculated transverse energy spectra for $Z=7$ and $Z=8$ at different incident energies. The experimental results are shown by different symbols for the different incident energies and the calculated spectra are shown by different histograms, indicated in the left figure. All spectra are given in an absolute differential cross section. Spectra are multiplied by a factor of 10^n $(n=0,1,2,3)$ from the bottom.

tions, however, overestimate the cross section at the high energy side of the IMFs both at 35*A* and 49*A* MeV. The calculations also underestimate the cross section for $Z=8$ at 69*A* MeV in the whole energy range, though the slope of the spectrum is rather well reproduced. Both in the experimental and calculated spectra no significant difference is observed between the spectra at all incident energies. As discussed below, however, the dissipated kinetic energy during collisions increases significantly as the incident energy increases.

According to Goldhaber [36], when the nucleus breaks into small fragments instantly, the momentum distribution of the fragments in the fragment rest frame is described by $\exp(-p^2/2\sigma^2)$ where

$$\sigma^2=\sigma_0^2K(A-K)/(A-1). \tag{8}$$

A is the parent mass and K is the fragment mass. σ_0 is related to the Fermi momentum p_F by $\sigma_0=\langle p^2\rangle/3=\langle p_F^2\rangle/5$. When the semitransperency and $p_F=230$ MeV/c are assumed, the transverse energy spectrum is described by $\exp(-E_t/T_0)$ with $T_0=9.3$ MeV for $K=15$. This is about a half of the experimentally observed slope. The harder slope reflects the expansion energy. The similarity of the transverse energy spectra at different incident energies, therefore, may suggest that the IMFs are produced at a slightly later stage or in the more central region after a significant amount of the excitation energy is removed by light particles.

G. Isotope distribution

Isotopes with $4\leqslant Z\leqslant 7$ were identified by the telescopes at 16.0°, 22.0°, and 28.5°. In Fig. 15 typical isotope yield distributions are shown at $\theta=28.5°$ for different incident

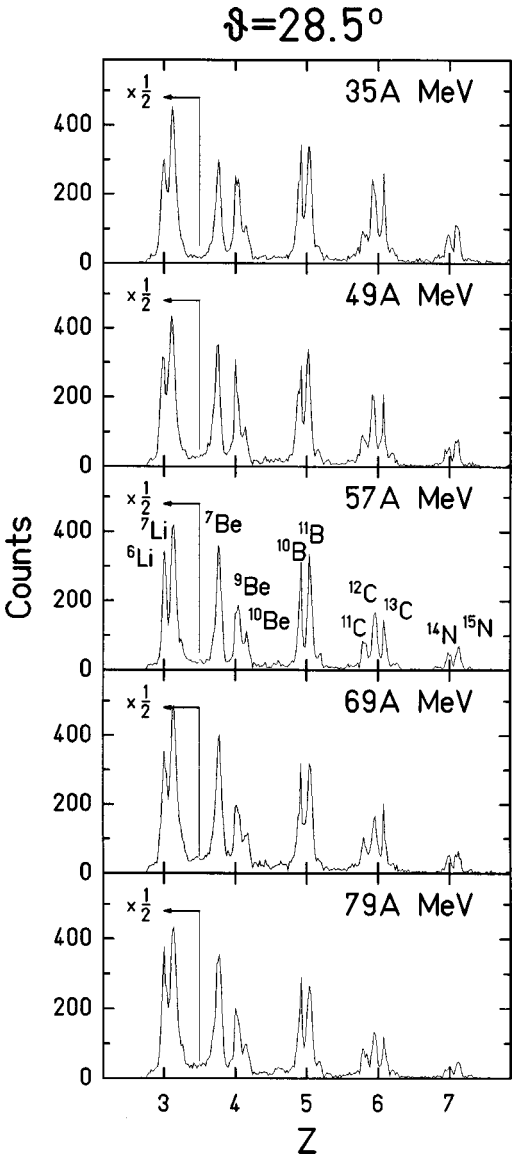

FIG. 15. Experimental yield distributions of the isotopes for IMFs with $4\leqslant Z\leqslant 7$ at $\theta=28.5°$ at different incident energies from 35*A* MeV (top) to 79*A* MeV (bottom). The *X* axis is the charge axis, used in the linealization process. Each peak corresponds to an isotope, assigned in the middle of the figure. The Li isotope yields are divided by a factor of 2 in all figures.

energies. An interesting observation is that no large change in the yield distribution for a given Z is observed for different incident energies. In Fig. 16, angle-integrated yield distributions are shown both for the exprimental and calculated results in different multiplicity windows at all incident energies. Beryllium isotopes show a systematic shift toward the neutron poor side, both in the experimental and calculated yield distributions, when the multiplicity decreases. This systematic change is observed at all incident energies except for 79*A* MeV. At 79*A* MeV, the distributions become more or less independent of the charged particle multiplicity both in the experimental and calculated results. Experimental yield distributions for other isotopes show much less dependence on the different multiplicity windows and on the different

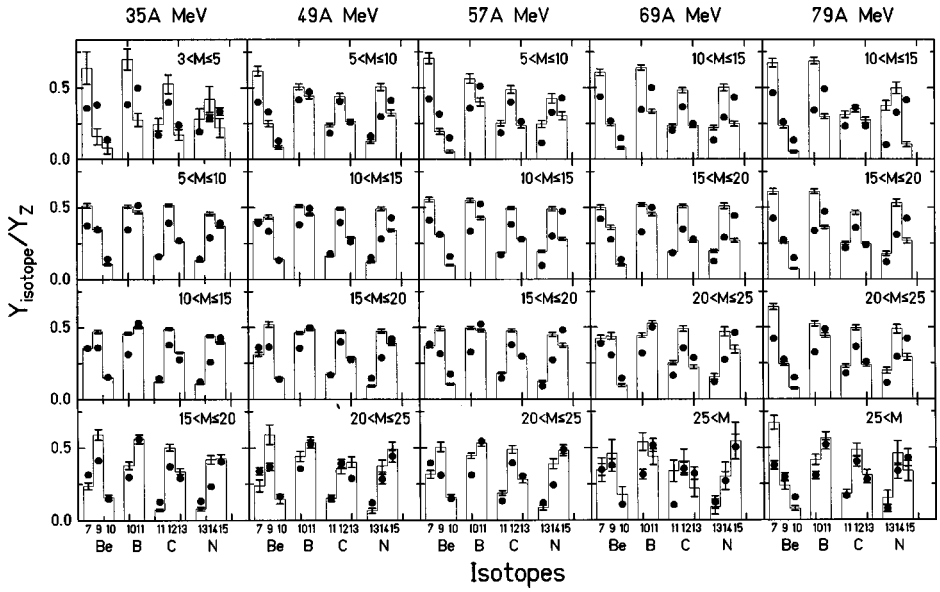

FIG. 16. Isotope distributions at 35*A* MeV (left column) to 79*A* MeV (right column) in different charged particle multiplicity windows. The range of the multiplicity window applied is indicated in each figure. Each point corresponds to the energy- and angle-integrated yield of an isotope, assigned on the *X* axis at the bottom figures. The experimental results are shown by dots and the calculated results are shown by histograms. Yields are normalized by the yield of all isotopes with a given charge. The error is the statistical error and indicated only for the calculated results. The experimental errors are about 2–3 times smaller than those of the calculations.

incident energies. The calculated yield distributions for boron and nitrogen isotopes, however, show a small systematic change from the lowest multiplicity window to the highest window. This change is almost identical for different incident energies. In general the essential trend of the experimental isotope yield distributions is well reproduced by the calculations and no systematic trend in the isotope yield distribution between different charges is observed both in the experimental and calculated results. This suggests that the primary isotope distributions are significantly modified by the decay and feeding processes of the fragments at later stages.

V. EXCESS CROSS SECTION IN THE MULTIPLICITY DISTRIBUTIONS

The calculated multiplicity distributions, shown in Fig. 2, significantly overestimate the experimental results at all incident energies. In order to elucidate the cause of the excess at $M\sim10$, contour plots of the light charged particle multiplicity versus the IMF multiplicity ($3\leqslant Z\leqslant 8$) are shown on the upper part of Fig. 17 for the reaction at 35*A* MeV. The experimental distribution is generally well reproduced by the calculation except for events in which no IMF is detected ($M_{IMF}=0$). In the lower part of the figures, the light charged particle multiplicity distributions are plotted separately for the events with $M_{IMF}=0$ and with $M_{IMF}=1$. In the experimental results the cross section for the events with no IMF increases monotonically when the multiplicity decreases. (Most events for $M_{LP}\leqslant 3$ were cut off by the hardware trigger during the experiment.) In the calculated results, on the other hand, a maximum is observed for the events with no IMF at $M_{LP}=8-9$ and the cross section is twice that of the experiment at the peak multiplicity. For the events with $M_{IMF}=1$ (dashed line histograms), the experimental cross section is reasonably reproduced in shape and magnitude by the calculation. The experimental cross sections for $M_{IMF}\geqslant 2$ are also well reproduced by the calculation, as seen in the upper figure. This observation indicates that the excess of the calculated cross section in the events with $M_{IMF}=0$ is directly reflected in the excess of the calculated cross section around $M\sim10$ in Fig. 2. In the upper part of

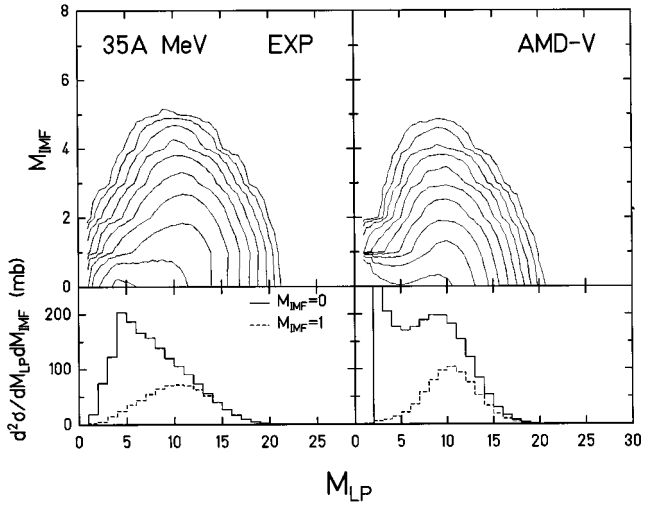

FIG. 17. Upper: contour plots of the multiplicity of the light charged particles with $Z=1$ and $Z=2$ versus the IMF multiplicity for the experiment (left) and for the calculation (right). Contours are on a logalithmic scale and each contour is different by a factor of 2. The same contour scale is used in both of the figures. Lower: light charged particle multiplicities for the events with $M_{IMF}=0$ (solid line histograms) and $M_{IMF}=1$ (dashed line histograms).

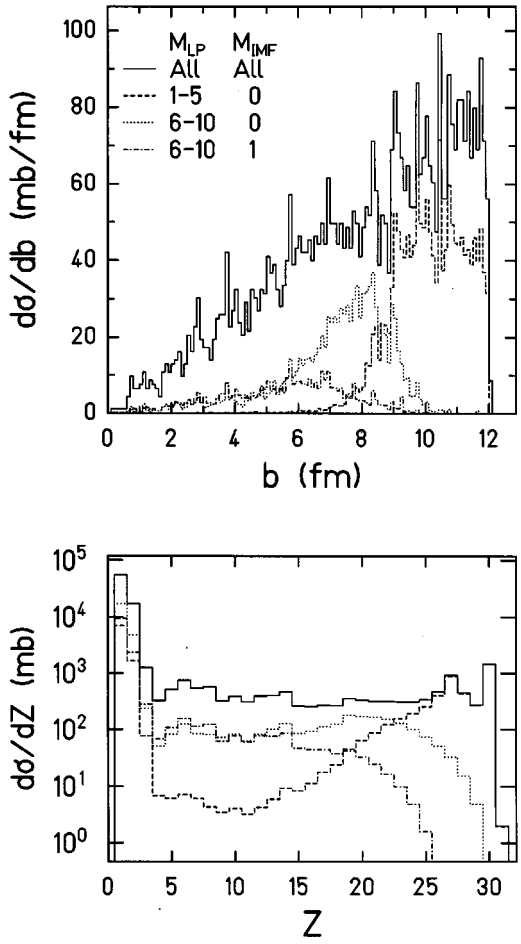

FIG. 18. Impact parameter distributions (upper) and charge distributions of fragments (lower) from the AMD-V calculation at 35*A* MeV are shown for different event types. The same line types are used in both figures for different event types. Solid line histograms indicate the distributions for all of the events. Dashed line histograms are for the events with $M_{IMF}=0$ and $6\leqslant M_{LP}\leqslant 10$, dotted line histograms are for the events with $M_{IMF}=0$ and $1\leqslant M_{LP}\leqslant 5$, and dot-dashed line histograms are for the events with $M_{IMF}=1$ and $6\leqslant M_{LP}\leqslant 10$. No experimental filter is applied for these events.

Fig. 18, impact parameter distributions are shown for different types of the calculated events at 35*A* MeV. The impact parameter distributions shift to a smaller value when M_{LP} and/or M_{IMF} become larger. The events with $M_{IMF}=0$ and $6\leqslant M_{LP}\leqslant 10$ are found to originate mainly from the impact parameter range of $b=7-8$ fm. In the lower part of figures the calculated charge distributions are shown. The charge distribution for the events with $M_{IMF}=0$ and $1\leqslant M_{LP}\leqslant 5$ show a peak near the projectile. The distribution for the events with $M_{IMF}=0$ and $6\leqslant M_{LP}\leqslant 10$ shows a broad peak around $Z\sim 20$. At $Z\leqslant 15$ the charge distribution for the events with $M_{IMF}=1$ and $6\leqslant M_{LP}\leqslant 10$ is very similar to that of $M_{IMF}=0$ and $6\leqslant M_{LP}\leqslant 10$, but drops more rapidly for larger Z values. These observations indicate that the events in the excess of the calculated cross section originate in collisions with an impact parameter range of 7–8 fm and result mostly with a large fragment with $Z\sim 20\pm 5$, which is not detected in the experiment because of the experimental conditions. In such collisions two nuclei collide only near the surface and the excess of the calculated cross section may be caused by the surface properties of the initial nuclei used in the AMD-V calculations.

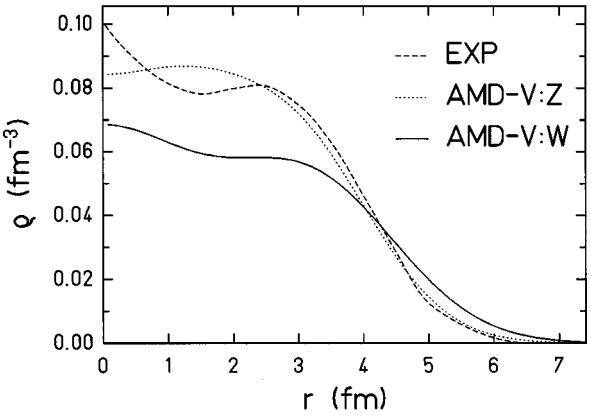

FIG. 19. Charge density distributions of ^{58}Ni. The dashed curve is the experimental result obtained from an electron elastic scattering experiment. The dotted curve is that of the initial nucleus calculated from the AMD coordinate $\{Z_i\}$. The solid curve is the distribution calculated from the physical coordinate $\{W_i\}$. See details in the text.

The reactions with $b\sim 7-8$ fm are governed mainly by the nucleon-nucleon collisions at nuclear surfaces. In the AMD-V model, the nucleon-nucleon collision is treated stochastically by using the physical coordinates $\{W_i\}$ in Eq. (4). The phase space distribution is assumed to have the form of Eq. (6) with this physical coordinate. Since this is valid only approximately, the density calculated from the physical coordinates $\{W_i\}$ slightly differs from that calculated from the AMD coordinates $\{Z_i\}$. For ^{58}Ni, the calculated charge density distributions using the AMD coordinates and the physical coordinates are shown by dashed and solid curves, respectively, in Fig. 19, compared to that of the experimental result [34]. The charge density distribution calculated from the AMD coordinates reproduces the experimental result rather well, whereas the density distribution calculated by the physical coordinates shows a much larger diffuseness. Since the reactions at collisions with $b\sim 7-8$ fm originate mainly from nucleon-nucleon collisions at the surface area of the initial nuclei, the imperfectness of the transformation from the AMD space to the physical coordinate space is likely to cause the excess cross sections in Fig. 2 and the discrepancies of the charge distributions in the lowest multiplicity window in Fig. 13. One should note, however, that the physical coordinate $\{W_i\}$ is only used for the stochstic nucleon-nucleon collision process and the equation of motion is entirely solved in the AMD space. The development of a more exact treatment of the physical coordinates is now under investigation.

VI. REACTION MECHANISM AND MULTIFRAGMENTATION

The AMD-V calculations reasonably reproduce all the essential features of the experimental results at all incident en-

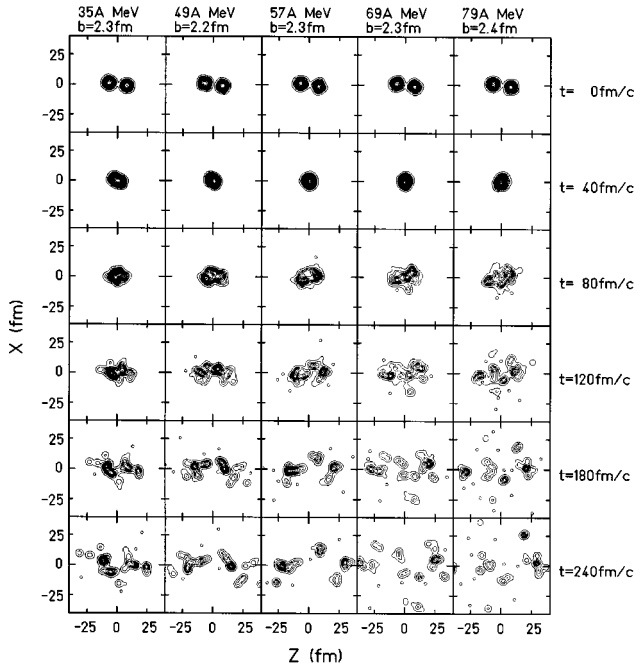

FIG. 20. Time evolution of nuclear density distributions, projected on the reaction plane (X-Z plane), for a calculated event with $b\sim 2.3$ fm at different reaction times for all incident energies. The incident energy is indicated at the top of each column with the impact parameter. The plots are made from the physical coordinates $\{W_i\}$. The plotted time is indicated on the right. The Z axis is taken as the beam direction and the contour scale is in linear. The smallest circle indicates a nucleon.

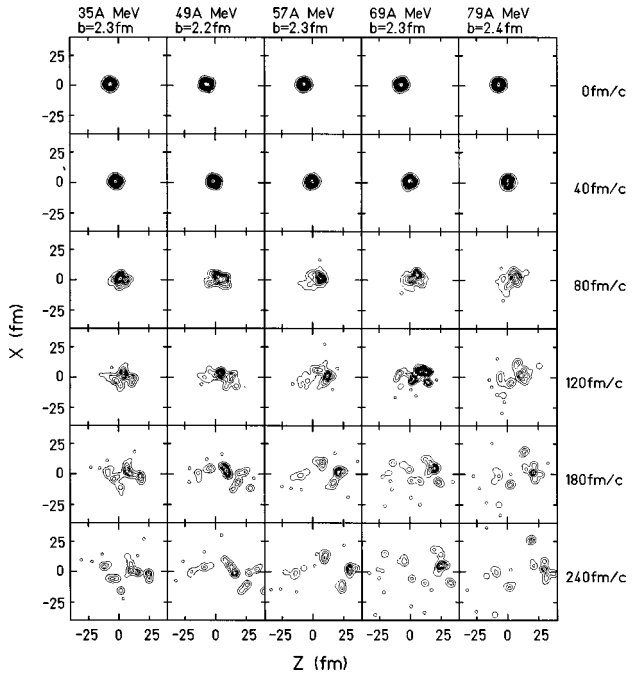

FIG. 21. Similar plots to Fig. 20 for the same events, but plotted only for the Gaussian wave packets in the projectile.

ergies, except for peripheral collisions. As a result the AMD-V calculation may provide further insights into the reaction mechanisms and the multifragment production processes for central or midcentral collisions. In order to perform such a detailed investigation, the properties of the Gaussian wave packets are examined during collisions. In this section all quantities are evaluated in the center-of-mass system. Some of the quantities are calculated by using only the wave packets which originate from nucleons of the projectile. In the following text such quantities are simply called quantities of the projectile in the center-of-mass system of these wave packets. The experimental filter is not applied to calculate the quantities. All reaction times depicted in this text start at a distance of 15 fm between two centers of the projectile and target in the beam direction. It takes ~ 15 fm/c at 35A MeV and ~ 10 fm/c at 79A MeV for the two nuclei to touch each other.

A. Multifragmentation

In Figs. 20 and 21 the time evolutions of the nuclear density distributions projected onto the reaction plane are shown for the whole system and for the projectile, respectively, for a collision with $b\sim 2.3$ fm at different incident energies. Both of the densities in Figs. 20 and 21 are calculated, using the physical coordinate $\{W_i\}$ to make it possible for a direct comparison. As seen in Fig. 20 the projectile and the target merge together around $t=40$ fm/c at all incident energies and stay as a single system only up to $t\sim 120$ fm/c at 35A MeV and $t\sim 80$ fm/c at 79A MeV. Preequilibrium nucleons appear by 180 fm/c at 35A MeV and by $t\sim 120$ fm/c at higher incident energies. The system starts to break into small pieces at $t\sim 180$ fm/c at 35A MeV and $t\sim 80$ fm/c at 79A MeV. The multifragmentation is a general feature for central or midcentral collisions in this reaction system at these incident energies. In Fig. 21 the time evolution for the projectile is shown. One can clearly see that a significant amount of nucleons and fragments are emitted in the forward direction after the multifragmentation process. A very similar observation was made in ^{40}Ca+^{40}Ca at 35A MeV [22].

B. Semitransparency

The observation in Fig. 21 indicates that a certain degree of the nuclear transparency exists. In the top row of Fig. 22, the average number of nucleons of the projectile or of the target, which cross $Z=0$ from one side to the other in the beam direction (Z direction), is plotted as a function of time. The number is evaluated by averaging over the events with $b\leqslant 3$ fm and scaled by the number of nucleons in each initial nucleus. For all the cases about 75% of nucleons on average appear on the opposite side. In order to study this transparency further during the collisions, contour plots of the average nuclear density, projected on the Z axis, versus reaction time are made for central events and shown in the lower part of Fig. 22. Two ridges merge together at ~ 40–50 fm/c, indicating that the projectile and the target form a single composite system. The slopes of these ridges correspond to the incident velocity of each nucleus. When the incident energy is lower, the slope becomes steeper. After the two nuclei merge together, the ridges still remain,

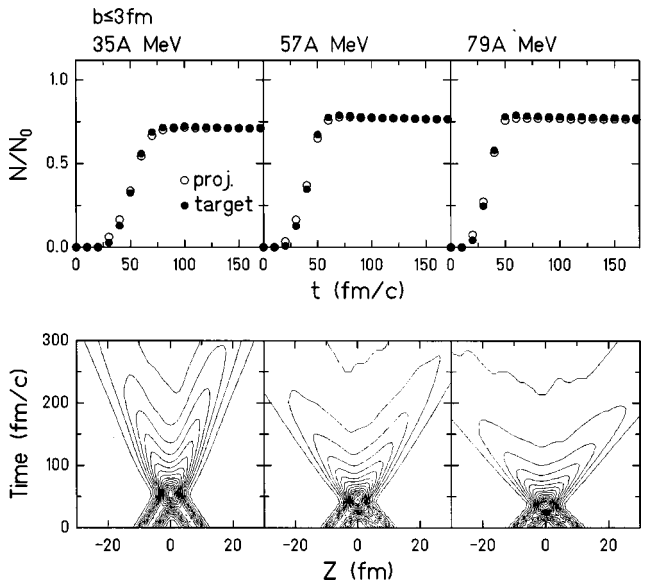

FIG. 22. Upper: the average number of nucleons in the initial nuclei across $Z=0$ from one side to the other is plotted as a function of time for three different incident energies. The average is taken over the events with $b\leqslant 3$ fm. The incident energy is indicated at the top of each figure. The extracted number is scaled by the number of nucleons in each nucleus. Lower: average nuclear density, projected on the Z axis, vs time is plotted for the same events. The contour scale is linear and arbitrarily normalized.

consistent with the above observation. This transparency, however, is quite different from those seen in the heavy ion simulations in time-dependent Hartree-Fock calculations at low incident energies [37]. First of all, the density of these ridges disappears gradually with the reaction time. This indicates that the projectile and target nuclei break into small pieces and spread widely along the ridges. Second, the slope of the ridges is steeper than that of the incident nuclei. This indicates that the projectile and target are slowed down during the collisions. In the nucleon transport, the reaction shows a transparency, whereas in the energy transport the reaction is much less transparent. We therefore designate this as semitransparency in the text. A similar observation has been made recently in a QMD simulation for Xe+Sn [20].

C. Average properties of the reaction and energy dissipation

In Fig. 23 the average quantities of the collisions at 35A MeV are plotted as a function of time for different impact parameter ranges. Each quantity is extracted by averaging over all events generated by the AMD-V model for a given impact parameter range. In the top row the average mass of the largest fragment is plotted. The average mass is calculated at each time step, using a coalescence radius of 5 fm in the spatial physical coordinate. The time evolution of the mass of the largest fragment for 0 fm$\leqslant b\leqslant$2 fm indicates that, at an early stage of the reaction, the projectile and the target merge together and form a composite system of mass around 120. The mass of the largest fragment decreases rapidly during the time interval of 100 fm/$c\leqslant t\leqslant$200 fm/c and changes slowly after that. The average mass of the largest fragment at $t=300$ fm/c is about 35. This number indicates that the system breaks into at least four or five pieces on average at $t=300$ fm/c. When the impact parameter increases, the average mass of the largest fragment becomes $\sim$50 at $t=300$ fm/c for 6 fm$\leqslant b\leqslant$8 fm. This reflects the fact that the binary nature of collisions is enhanced for more peripheral collisions. In the second row the numbers of two nucleon collisions are plotted both for the attempted and the Pauli allowed collisions. About 10% of collisions are Pauli allowed during the reaction. The number of collisions peaks around $t=40$ fm/c. For central collisions, about 40 collisions are allowed during the early stage of the reaction ($0\leqslant t\leqslant 70$ fm/c). The number of collisions decreases when the impact parameter increases. The 10% of the allowed rate stays the same in later stages. This indicates that, in these later stages, clusters are formed and most collisions occur inside the clusters. In the third row the average excitation energy per nucleon is plotted for the maximum mass fragment. The excitation energy is calculated from the total internal energy by subtracting the binding energy. The excitation energy reaches about 8A MeV in the early stage and rapidly decreases between 100 fm/c and 200 fm/c. After $t\sim$200 fm/c the excitation energy decreases slowly and becomes about 3A MeV at $t\sim$300 fm/c for all impact parameter ranges. One should note, however, that the maximum excitation energy at the early stage of the reaction does not necessarily indicate that the system reaches the ''hottest'' stage, because the system is not yet thermalized at this time. At the time of the maximum excitation energy, as discussed below, most of the projectile nucleons are still moving along the beam direction. The calculated excitation energy, therefore, includes a large amount of this kinetic energy. This is not the case at the later stage ($t\geqslant$200 fm/c). After the system breaks into small pieces and the interaction between fragments ceases, nucleon motion in a fragment becomes random. The calculated internal energy, therefore, shows the thermal excitation energy properly in the later stage. In the fourth row the time evolution of dissipated energy is shown. The dissipated energy is an alternative presentation of the excitation energy, commonly used for the heavy ion collisions at low energies. The dissipated energy is calculated from the parallel momentum of the projectile wave packets as follows:

$$E_{diss}=E_0-2\frac{\left(\sum_i^{A_p} P_\parallel^i\right)^2}{2M_p}, \tag{9}$$

where E_0 is the sum of the kinetic energy of the projectile and target in the center-of-mass system at $t=0$ fm/c. $P_\parallel^i$ is the parallel momentum of the centroid of the ith Gaussian wave packet and the summation is made over all wave packets in the projectile. A_p and M_p are the mass number and mass of the projectile, respectively. A factor of 2 is multiplied in the second term to take into account the wave packets both in the projectile and the target nuclei. The dissipated energy is zero at $t=0$ fm/c by definition and increases when a reaction occurs and reaches the maximum around t

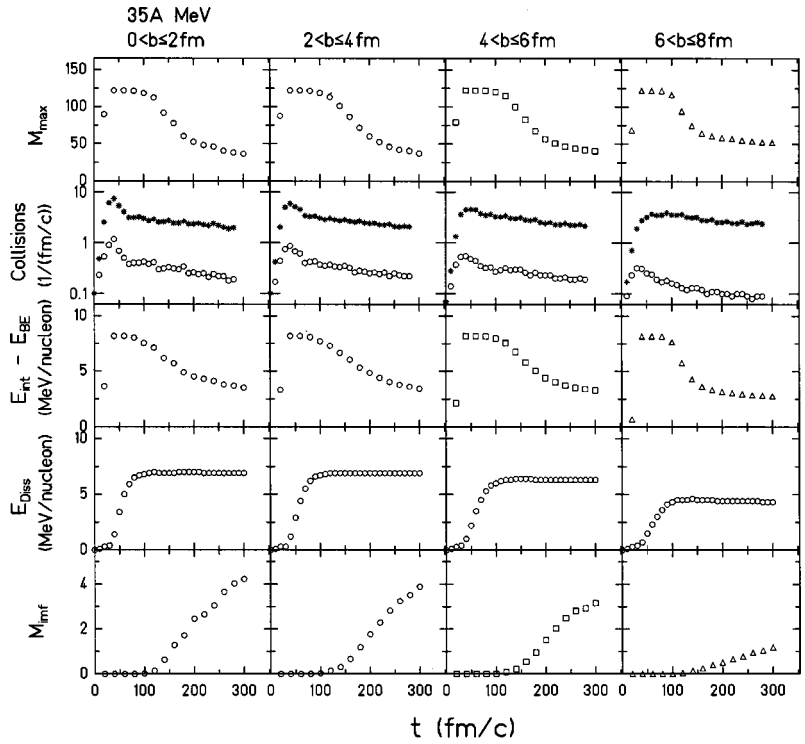

FIG. 23. Average properties of the reaction at 35*A* MeV for different impact parameter ranges, indicated at the top of each column. From the top row to the bottom, the maximum mass, the number of collisions, the excitation energy, the dissipated energy, and the multiplicity of IMFs ($3 \leqslant Z \leqslant 15$) are plotted as a function of the reaction time. In the second row, the number of attempted collisions per unit time is shown by dots and the number of Pauli-allowed collisions is shown by circles.

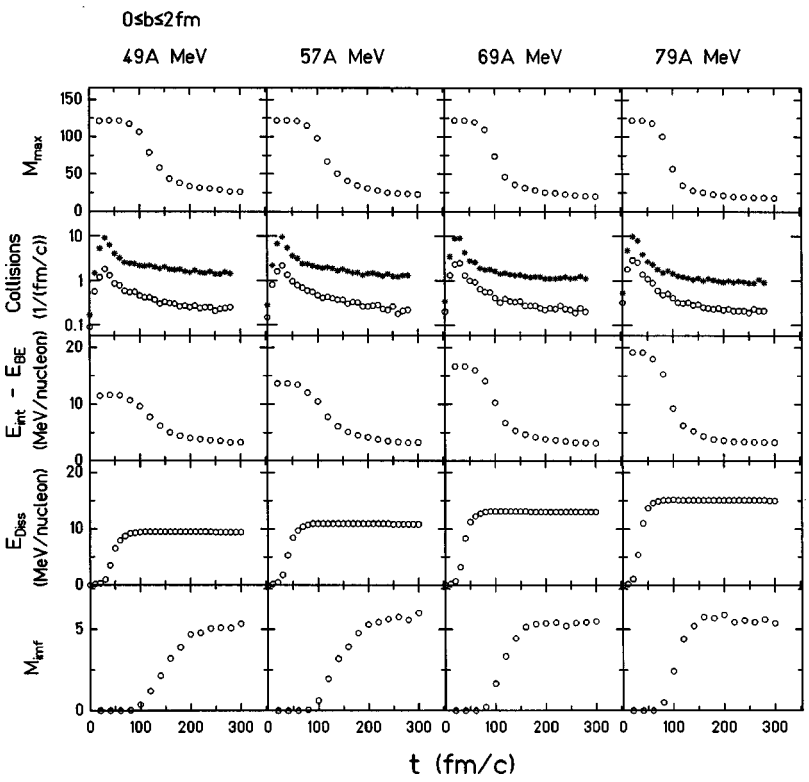

FIG. 24. Similar plots to those in Fig. 23, but for the most central events (0 fm$\leqslant b \leqslant$2 fm) at different incident energies, indicated at the top of each figure.

$=80$ fm/c for all impact parameter ranges and remains constant after that. The maximum dissipated energy is about 7A MeV for the most central collisions. This energy corresponds to about 80% of the available initial kinetic energy. The maximum dissipated energy significantly decreases when the impact parameter increases. One should note that the dissipated energy reaches its maximum at slightly later time than the excitation energy in the third row does. This will be discussed in the next section in more detail. In the bottom row the time evolutions of the average multiplicities of IMFs ($3 \leqslant Z \leqslant 15$) are plotted. The multiplicity increases rapidly at $t=120$ fm/c for central collisions. The maximum multiplicity of IMF's decreases gradually when the impact parameter increases.

In Fig. 24 similar plots to those in Fig. 23 are shown for the most central collisions at higher incident energies. The average mass of the largest fragment at $t=300$ fm/c decreases gradually from 25 at 49A MeV to 20 at 79A MeV. The peak rate of Pauli-allowed collisions increases from 1.8/(fm/c) at 49A MeV to 2.9/(fm/c) at 79A MeV, though the number of attempted collisions remains more or less constant. This is reasonable because the available phase space increases and more collisions are Pauli allowed with increasing incident energy. On the other hand, the number of the attempted collisions remains constant because the number is mainly determined by the geometrical sizes of the system and the impact parameter. The average excitation energy of the maximum fragment at $t=300$ fm/c stays rather constant at $\sim 3A$ MeV for all cases. The excitation energy of 3A MeV at $t=300$ fm/c is consistent with the result of Marie *et al.* [38] for the fragment excitation energy. In their work the Xe + Sn reaction at 50A MeV was studied and the excitation energy of a fragment was determined by extracting the multiplicity of the light charged particles emitted from the fragment. The fragment excitation energy of 3.0A MeV was obtained by comparing the observed multiplicity with results of a statistical model calculation. The average dissipated energy in the fourth row increases significantly from 9.5A MeV at 49A MeV to 15A MeV at 79A MeV. This increase, however, is not reflected on the fragment excitation energy at the later stage. Another interesting observation is that the ratio between the total dissipated energy and the initial kinetic energy stays more or less constant. About 80% of the initial kinetic energy is dissipated during the collisions for all incident energies studied here. IMF multiplicity reaches a plateau at progressively earlier times when the incident energy increases. The plateau starts at $t \sim 200$ fm/c at 49A MeV and $t \sim 150$ fm/c at 79A MeV. The multiplicity at the plateau is similar for the different incident energies.

D. Dynamics of the multifragmentation process

In Fig. 25 the time evolution of the nuclear density and momentum distributions for a central event at 35A MeV are shown for expanded scales in space and time. In these plots the distributions are plotted from the wave packets only near the reaction plane. Two nuclei merge together at $t=50$ fm/c as seen in the left column. At this time, however,

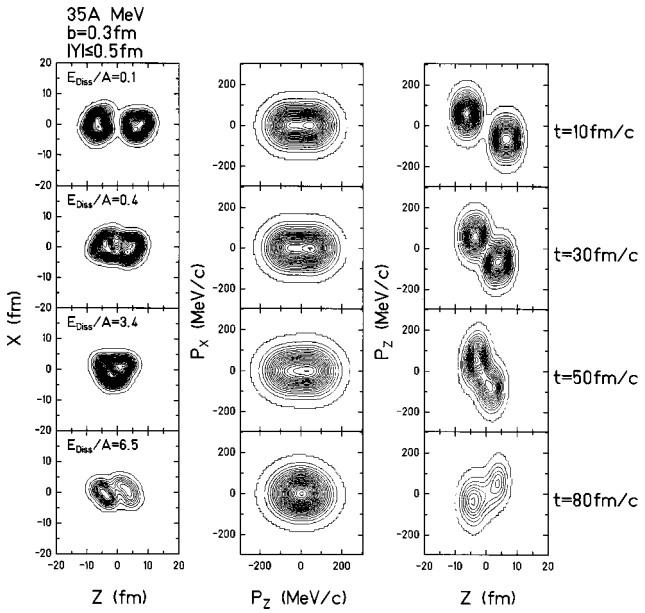

FIG. 25. Left: time evolution of the nuclear density distribution in the X-Z plane for Gaussian wave packets near the reaction plane (-0.5 fm$\leqslant Y \leqslant 0.5$ fm) is plotted for a central event with $b=0.3$ fm at 35A MeV. The plotted time is indicated on the right. The average dissipated energy at the given time is also given in each figure. Middle: time evolution of the momentum distribution in the X-Z plane for the Gaussian wave packets of the same set plotted on the left. Right: time evolution of the phase space distribution projected in the P_Z-Z plane for all of the Gaussian wave packets. All contour scales are linear and arbitrarily normalized.

the momentum distribution in the middle column still shows an ellipsoid stretched in the beam direction. The average dissipated energy is 3.4A MeV, which is about a half of the maximum dissipated energy reached at $t \geqslant 100$ fm/c. The momentum distribution becomes closer to a spherical shape at $t=80$ fm/c, but the projectile still has about 20% of the initial kinetic energy on the beam direction. At this time about 75% of the projectile wave packets are passing through the target nuclei, as seen in the top row of Fig. 22, and the entire system is ready to break into small pieces. In the right column phase space distributions are shown. One can clearly see that the projectile wave packets are still moving along the beam axis at the time of the full overlap and continuing to move to the same direction. A two-peak structure in the phase space at 80 fm/c indicates that the energy dissipation is incomplete and the system has no chance to bounce back to a single source. The essential feature of the above observations remains the same for the reactions at higher incident energies.

In order to further study the dynamics of multifragmentation, the maximum nuclear density and radial flow momenta are investigated as a function of time for central events. The maximum nuclear density of the system is calculated exactly from the AMD coordinate $\{Z_i\}$ in these plots. The extracted values are normalized by the normal nuclear density $\rho_0 = 0.163$ fm^{-3}. The radial flow momenta are calculated in the projectile rest frame in order to isolate the radial flow from the other kinetic energy contributions. The radial flow

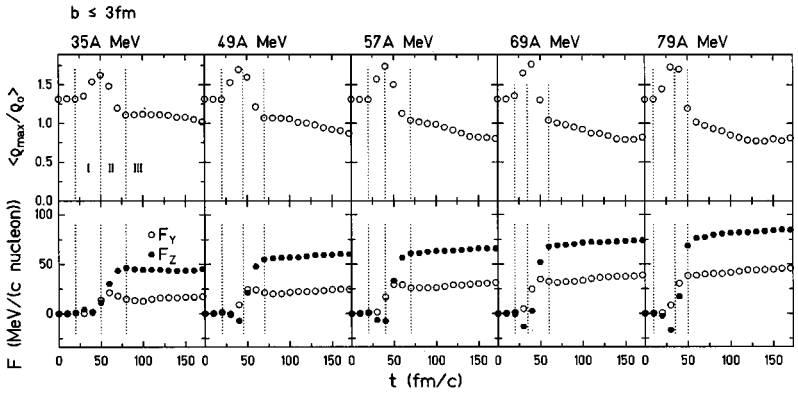

FIG. 26. Average maximum nuclear density (upper) and the radial flow momenta in the projectile (lower) are plotted as a function of the reaction time for central events (0 fm$\leqslant b \leqslant 3$ fm) at all incident energies. The incident energy is indicated on the top of each column. Vertical dashed lines in each figure indicate three different phases in time, discussed in the text. In the lower figures dots indicate the radial flow momentum F_Z in the beam direction and circles indicate F_Y in the direction perpendicular to the reaction plane.

is studied in two directions: the perpendicular direction to the reaction plane (Y direction) and the parallel direction to the beam axis (Z direction). Radial flow momenta F_Y and F_Z are defined as

$$F_Y = \frac{1}{A_p} \sum_{i=1}^{A_p} \mathrm{sgn}(Y) P_Y , \tag{10}$$

$$F_Z = \frac{1}{A_p} \sum_{i=1}^{A_p} \mathrm{sgn}(Z) P_Z . \tag{11}$$

A_p is the mass number of the projectile and the summation is taken over all the wave packets in the projectile. F_Y and F_Z are evaluated by averaging over all events in a given impact parameter range. A positive (or negative) value of the flow momentum indicates that, on average, the wave packet is moving outward (or inward) and therefore the projectile is expanding (shrinking).

The calculated results are shown in Fig. 26 for the events with $b \leqslant 3$ fm. The time evolution of the maximum nuclear density, shown at the upper row, is very similar at all incident energies. The density reaches a peak at an early stage, when the two nuclei are overlapped, and then returns to a density close to the normal nuclear density. In order to study the multifragmentation process in detail, three phases are introduced in the reaction time, shown by the vertical dotted lines in the figures. Phase I is the time period from the time when two nuclei touch each other to the time when the two nuclei are fully overlapped. Phase II is the time period at the time of the overlap to the time when the maximum density returns to the normal nuclear density, and phase III is attributed to the time period after that. The average maximum nuclear density at $t=0$ fm/c is 1.3, reflecting the internal density distribution of the initial nucleus as seen in Fig. 19 for the charge distribution. The density reaches the maximum of about $1.6\rho_0$ at $t=50$ fm/c at $35A$ MeV and the maximum increases only slightly when the incident energy increases. The density reaches about $1.7\rho_0$ at $79A$ MeV. The maximum nuclear density in phase III is determined by the density in fragments. At $35A$ MeV the density reaches the lowest value of $0.9\rho_0$ at $t=230$ fm/c (which is not shown) and gradually return to the normal density. At $79A$ MeV, the density reaches the lowest value of $0.8\rho_0$ at $t=130$–140 fm/c and returns to $0.9\rho_0$ at $t=300$ fm/c.

In the lower row of Fig. 26, the time evolution of the radial flow momentum of the projectile is shown. At $35A$ MeV, the radial flow momentum of the projectile stays zero in phase I and starts to increase at the end of phase I, just before the two nuclei are fully overlapped. The increase rate of the radial flow in the Y and Z directions is very similar, suggesting that the projectile expands thermally. In phase III the projectile expands more or less at a constant velocity, although the radial flow momentum F_Z in the beam direction is twice larger than that of the Y direction. This difference suggests that the projectile is slightly stretched in the beam direction during the semi transparent process. At $49A$ MeV the situation is slightly different from that at $35A$ MeV. At the end of phase I the radial flow momentum F_Y starts to become positive, whereas F_Z first becomes negative. This indicates that the projectile starts to expand in the Y direction, whereas the projectile is compressed in the beam direction at this time. This compression results in the faster expansion in the beam direction in phase II and the slightly larger values of the resultant radial flow momenta in phase III, compared to those at $35A$ MeV. The increase rate of F_Y is similar to that at $35A$ MeV, suggesting the expansion in the Y direction is thermal. In phase III, the difference between F_Z and F_Y is similar to that at $35A$ MeV, indicating that a similar stretch of the projectile occurs in the beam direction during the semitransparent process. At higher incident energies, the characteristic features of the expansion process are essentially the same as that at $49A$ MeV. The negative value of F_Z increases gradually when the incident energy increases, indicating that more compression occurs at the higher incident energies. As a result the expansion rate increases in phase II and the resultant F_Y and F_Z also in-

creases in phase III. The difference of the radial flow momenta F_Z and F_Y stays more or less constant.

The compression mechanism at higher incident energies can be qualitatively understood as follows. The nuclear density during the collisions is governed by two factors. One is the mean field and the other is the two-nucleon collision process. When the projectile nucleons enter into the target mean field in phase I, they are accelerated by the attractive mean field and the projectile tends to be stretched in the beam direction. At the same time, on the other hand, two-nucleon collisions occur and the projectile nucleons are slowed down. At 35*A* MeV, these two processes are more or less balanced and F_Z stays zero. At 49*A* MeV and higher energies, the mean field acceleration becomes slightly smaller because the interaction time is shorter. On the other hand, the deceleration process by the two-nucleon collisions becomes more significant because the number of the Pauli-allowed collisions increases and the momentum transfer in a collision also increases. As a result the density compression occurs in the beam direction at the higher energies.

VII. SUMMARY

Energy spectra and energy integrated angular distributions of IMFs, *Z* distributions, and isotope distributions, classified by the associated charged particle multiplicity, have been studied at different incident energies between 35*A* MeV and 79*A* MeV. All experimental results have been compared with AMD-V calculations. The experimental energy spectra show little dependence on the associated charged particle multiplicity at a given incident energy. All experimental angular distributions of IMFs show a forward peak around $\theta \sim 7°-10°$ and show only slight differences for the different multiplicity windows and for the different incident energies. Charge distributions of fragments change systematically for the different multiplicity windows at a given incident energy. Isotope yield distributions of IMFs with a given charge also depend only slightly on the different multiplicity windows and on the different incident energies. The AMD-V calculations reasonably well reproduce the essential features of the above experimental results and provide insight into the reaction mechanisms and the fragmentation processes. The AMD-V model predicts multifragmentation at all incident energies studied here, in agreement with the experimental observations. A semitransparency is predicted at all incident energies even for central collisions. About 75% of the projectile nucleons pass through the target nucleus and appear in the forward direction with a significant energy dissipation. The dynamics of the multifragmentation process is also studied in detail using the calculated events. The detailed study suggests that, at 35*A* MeV, thermal expansion and the semitransparency are the dominant mechanisms for the multifragmentation process, whereas, at 49*A* MeV and the higher incident energies, nuclear compression occurs and plays an important role in the multifragmentation process in addition to the thermal expansion and the semitransparency.

ACKNOWLEDGMENTS

We thank the staff of the GANIL Accelerator facility for their support during the experiment. We also thank Dr. R. J. Charity for providing us the GEMINI code. We further acknowledge Dr. I. Tanihata and Dr. Y. Yano for the convenience to use the RIKEN VPP700E Supercomputer facility. This work was supported by the U.S. Department of Energy under Grant No. DE-FG03-93ER40773 and the Robert Welch Foundation.

[1] L. G. Moretto and G. L. Wozniak, Annu. Rev. Nucl. Part. Sci. **43**, 379 (1993) and references therein.
[2] D. R. Bowman *et al.*, Phys. Rev. C **46**, 1834 (1992).
[3] M. B. Tsang *et al.*, Phys. Rev. Lett. **71**, 1502 (1993).
[4] K. Hagel *et al.*, Phys. Rev. C **50**, 2017 (1994).
[5] M. F. Rivet *et al.*, Phys. Lett. B **388**, 219 (1996).
[6] B. Borderie *et al.*, Phys. Lett. B **388**, 224 (1996).
[7] N. Marie *et al.*, Phys. Lett. B **391**, 15 (1997).
[8] M. Louvel *et al.*, Nucl. Phys. **A559**, 137 (1993).
[9] D. Cussol *et al.*, Nucl. Phys. **A561**, 298 (1993).
[10] R. Wada *et al.*, Phys. Rev. C **39**, 497 (1989).
[11] D. H. Gross, Rep. Prog. Phys. **53**, 605 (1990).
[12] A. S. Botvina, A. S. Iljinov, I. N. Mishustin, J. P. Bondorf, R. Donangelo, and K. Sneppen, Nucl. Phys. **A475**, 663 (1987).
[13] J. P. Bondorf, A. S. Botvina, A. S. Iljinov, I. N. Mishustin, and K. Sneppen, Phys. Rep. **257**, 133 (1995).
[14] W. A. Freedman, Phys. Rev. C **42**, 667 (1990).
[15] A. Bonasera, F. Gulminelli, and J. Molitoris, Phys. Rep. **243**, 1 (1994).
[16] K. Hagel *et al.*, Phys. Rev. Lett. **68**, 2141 (1992).
[17] B. Borderie *et al.*, Z. Phys. A **338**, 369 (1991).
[18] R. Wada *et al.*, Phys. Rev. C **55**, 227 (1997).
[19] J. Cibor *et al.*, Phys. Rev. C **55**, 264 (1997).
[20] R. Nebauer and J. Aichelin, Nucl. Phys. **A650**, 65 (1999).
[21] A. Ono and H. Horiuchi, Phys. Rev. C **53**, 2958 (1996).
[22] R. Wada, K. Hagel, J. Cibor, J. Li, N. Marie, W. Q. Shen, Y. Zhao, J. B. Natowitz, and A. Ono, Phys. Lett. B **422**, 6 (1998).
[23] H. Feldmeier, Nucl. Phys. **A515**, 147 (1990).
[24] J. C. Steckmeyer *et al.*, Phys. Rev. Lett. **76**, 4895 (1996).
[25] G. Bizard *et al.*, Nucl. Instrum. Methods Phys. Res. A **244**, 483 (1986).
[26] A. Péghaire *et al.*, Nucl. Instrum. Methods Phys. Res. A **295**, 365 (1990).
[27] F. Hubert, R. Bimbot, and H. Gauvin, At. Data Nucl. Data Tables **46**, 1 (1990).
[28] A. Ono, H. Horiuchi, Toshiki Maruyama, and A. Ohnishi, Prog. Theor. Phys. **87**, 1185 (1992).
[29] A. Ono, Phys. Rev. C **59**, 853 (1999).
[30] J. Dechargé and D. Gogny, Phys. Rev. C **21**, 1568 (1980).
[31] A. Ono and H. Horiuchi, Phys. Rev. C **53**, 2341 (1996).
[32] R. J. Charity *et al.*, Nucl. Phys. **A483**, 371 (1988).

[33] S. Kox, A. Gamp, R. Cherkaoui, A. J. Cole, N. Longequeue, J. Menet, C. Perrin, and J. B. Viano, Nucl. Phys. **A420**, 162 (1984).
[34] H. De Vries, C. W. De Jager, and C. De Vries, At. Data Nucl. Data Tables **36**, 495 (1987).
[35] T. Li *et al.*, Phys. Rev. Lett. **70**, 1924 (1993).
[36] A. S. Goldhaber, Phys. Lett. **53B**, 306 (1974).
[37] M. Prakash, S. Shlomo, B. S. Nillson, J. P. Bondorf, and F. E. Serr, Nucl. Phys. **A385**, 483 (1982).
[38] N. Marie *et al.*, Phys. Rev. C **58**, 256 (1998).